3D vs. 2D Channel Capacity of Outdoor to Indoor Scenarios Derived from Measurements in China and New Zealand

Yawei Yu*, Jianhua Zhang*, Mansoor Shafi†
*Beijing University of Posts and Telecommunications, Beijing, China.
†Spark New Zealand, Wellington, New Zealand.
email: {yyw,jhzhang}@bupt.edu.cn, mansoor.shafi@spark.co.nz

***Abstract*—Three dimensional (3D) Multiple Input Multiple Output (MIMO) is considered as one key technology for 5th Generation mobile communication systems. However, can the capacity derived from a 3D channel impulse response (CIR) better approximate the corresponding capacity derived from the measured CIR? Is there a substantial improvement in the capacity of 3D MIMO system in comparison to the classical 2D case? To answer these questions, extensive field measurements were conducted for the outdoor to indoor scenarios in China and New Zealand. Key channel parameters are extracted from the measured channel impulse response via the space-alternating generalized expectation-maximization algorithm, followed by the reconstruction of the 32 $\times$ 56 CIR according to 2D and 3D channel model. Then CIRs are used to evaluate the channel capacity and comparative simulation results demonstrate that the 3D MIMO capacity closely approximates the capacity predicted with practical CIRs. Moreover, obvious enhancements in the capacity of 3D channel is observed in comparison to 2D case. In addition, the distribution of eigenvalues and the number of contributing eigenvalues are also investigated.**

I. Introduction

It is estimated that global International Mobile Telecommunications (IMT) traffic will grow by 10-100 times from 2020 to 2030, a 10 Gbps peak rate is required [1]. To fulfill this demand, a lot of research activities are taking place under the umbrella of 5th generation mobile communication systems [2]. Among these, one important area is 3 dimensional (3D) Multiple Input Multiple Output (MIMO), which in addition to the azimuth domain, also takes the elevation domain into consideration, thus providing additional degrees of freedom to meet the high capacity demand [3].

An early research on the elevation angle consideration can be traced back to 1979 by Aulin, who extended Clark's scattering model to 3D space [4]. By including the vertical component, the 2D spatial channel model (SCM) [5] was extended to a 3D model and the ergodic capacity of the pure 3D propagation environment was shown to almost double the corresponding value for the 2D case [6]. By using a 3D MIMO antenna array with 32 elements instead of a 2 port linear antenna array, 23.6 times the average cell throughput gain and 1.55 times the cell edge throughput gain can be achieved [7]. Researchers now rely on the great promise of 3D MIMO to improve the capacity of future wireless systems. However, all of the above research is based on simulations of well known channel models, such as the 3GPP SCM and World Wireless Initiative New Radio + (WINNER+) [8], rather than real measurements. Therefore a validation for the above conclusions is needed from the real environments. In [9], Koppenborg et al. initiated the lab and field trails to assess whether the predicted 3D MIMO performance gain can be achieved in the real propagation environments, and proved that in the real environments even with hardware limitation, 3D MIMO may still offer better performance compared to the 2D case. However, no quantitative result was given.

In this paper, we report the measurement results under outdoor to indoor (O2I) scenario in China and New Zealand (NZ) with 32 antennas at transmitter (Tx) and 56 antennas at receiver (Rx). Key channel parameters were extracted via spatial-alternating generalized expectation-maximization (SAGE) algorithm [10]. Followed by this, we reconstruct a 2D channel channel impulse response (CIR) and 3D CIR, respectively. Further more, we predict the channel capacity and present comparative performance of capacity and eigenvalues distributions between 2D and 3D channels.

The remainder of this paper is outlined as follows. Section II gives a detailed descriptions of the measurement equipment and scenario, followed by the specific data post-processing and channel reconstruction in Section III. Capacity calculation and eigenvalue distributions are presented in Section IV, along with the results and detailed analysis in Section V. Finally conclusions are presented in Section VI.

II. Measurement Description

A. Measurement System

We conducted channel measurements in China and NZ, utilizing the Elektrobit Propsound Sounder described in [11]. To capture the propagation rays in the 3D environment efficiently, fully dimensional antenna arrays were equipped at both sides of the measurement link. The layout of the antenna arrays at Tx and Rx side are illustrated in Fig. 1(a) and Fig. 1(b), respectively. At the Rx, dual-polarized omnidirectional array (ODA) consisting of 56 antenna elements with 8 adjacent sides and a top surface was used, while a dual-polarized uniform planar array (UPA) with 32 antenna elements was utilized as a sector transmit antenna array. All array elements consisted of microstrip patches with 6 dB beamwidth of

978-0-9928-6265-7/16/$31.00 ©2016 IEEE

approximately 110^o in both the vertical and horizontal planes. The gain of each antenna element is 6 dBi, with an angle resolution of 2^o. This is limited by the sensors' distribution density in the anechoic chamber for antenna calibration, then angle information for paths can be extracted by substituting all possible angle values inside the antenna calibration file iteratively until the reconstructed signal best fits the actual received one [10]. Table I specifies the configuration and angle range of the antenna arrays along with other measurement parameters. The angle ranges capture most of the propagation paths at both ends of the link, where paths with a delay interval larger than the delay resolution can be distinguished. All antennas were calibrated in an anechoic chamber.

TABLE I
ANTENNA CONFIGURATION USED IN MEASUREMENTS

Parameter		Value	
Antenna type		ODA	UPA
Element number		56	32
Polarized		$\pm 45^o$	$\pm 45^o$
Distribution of antenna elements		cylinder	planar
Angle range	Azimuth	$-180^o \sim 180^o$	$-70^o \sim 70^o$
	Elevation	$-70^o \sim 90^o$	$-70^o \sim 70^o$

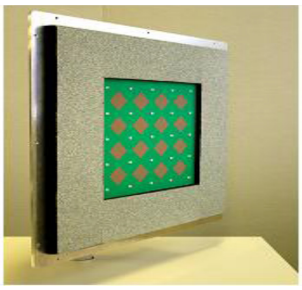

(a) Tx: 4×4 patches with each patch comprising a pair of corss-polarized antennas.

(b) Rx: 8 adjacent sides with 3 patches each, a top surface with 4 patches, each patch contains a pair of corss-polarized antennas.

Fig. 1. Antenna layouts used in the measurements.

B. Measurement scenarios

Using the same equipment, we carried out the field measurements under O2I scenario at carrier frequencies of 3.5 GHz and 2.35 GHz in China and NZ, respectively. The scenarios are illustrated in Fig. 2.

In China measurement in Fig. 2(a), the transmit antenna array is mounted at the top of the building with a height of 11.5 m to the ground, and the receiver, installed on a 1.78 m high trolley, collects channel responses inside a 15-floor building near the Tx side. The distance between these two buildings is 21.5 m and the 3rd floor faces the transmit antenna array rightly. The Rx was located in the 1st, 2nd, 3rd, 5th, 7th, 9th, 11th floor with a height of 4.0 m, 8.5 m, 12.0 m, 19.0 m, 26.0m, 33.0 m, 40.0 m, respectively. Totally 60 fixed spots

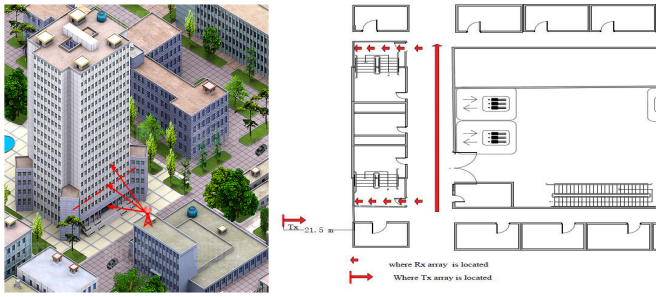

(a) Measurement in China

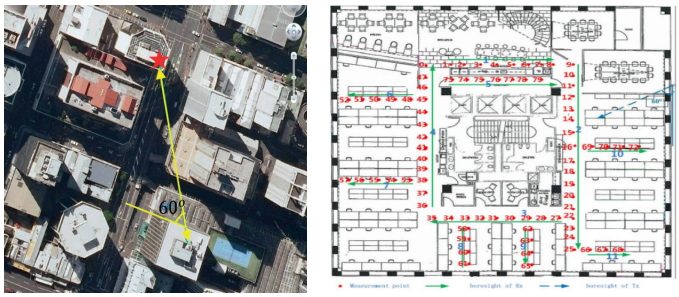

(b) Measurement in NZ

Fig. 2. A view of measurement areas in China (a) and NZ (b).

along the marked route were measured with 500 snapshots for each location.

The NZ measurement, shown in Fig. 2(b), was performed at a cell site with the Tx antenna installed on the rooftop of a 45 m high building with its boresight pointing to the measurement building (marked in red star), which is approximately 100 m far away. Approximately 80 fixed locations were measured, with 200 snapshots collected for each location.

III. Data Processing and Channel Reconstruction

A. Data processing

The field measurements described above provided numerous snapshots of time-varying CIR. Then collected CIRs were fed to a high-resolution algorithm to estimate the channel parameters for each snapshot. While maximum likelihood estimation (MLE) provides an optimum unbiased estimation from a statistical perspective, it is computationally prohibitive due to the multidimensional searches required. The SAGE algorithm has been proposed as a low-complexity approximation of MLE, and has been successfully applied to parameter estimation in channel sounding in recent years, which eliminates the antenna pattern effects while extracting practical channel propagation information.

B. Channel reconstruction

Consider a MIMO system with S transmit antennas and U receive antennas, the channel complex matrix $\mathbf{H}(t,\tau)$ of the resolvable delay τ at time t can be presented as

$$\mathbf{H}(t,\tau) = \sum_{l=1}^{L} \mathbf{H}_l(t) \cdot \delta(\tau - \tau_l(t)) \qquad (1)$$

where $\mathbf{H}_l(t)$ and τ_l are the channel complex matrix and the propagation delay of resolvable path l.

The channel complex matrix of the resolvable path l

$$\mathbf{H}_l(t) = \begin{pmatrix} h_{11,l}(t) & \cdots & h_{1s,l}(t) & \cdots & h_{1S,l}(t) \\ \vdots & \ddots & & & \vdots \\ h_{u1}(t) & & h_{us,l}(t) & & h_{uS,l}(t) \\ \vdots & & & \ddots & \vdots \\ h_{U1}(t) & \cdots & h_{Us,l}(t) & \cdots & h_{US,l}(t) \end{pmatrix} \quad (2)$$

is a $U \times S$ matrix whose entry $h_{us,l}(t)$ is the scalar valued response between the transmit antenna s and the receive antenna u. The channel reconstruction based on the practical antenna pattern heavily, U and S are set as 56, 32, respectively.

1) Filed measurements of CIR: Signals propagated through the channel are collected by the Rx and stored in the sounder in binary bits for both I data and Q data, thus the impulse response H_{IR} can be calculated as $H_{IR} = I + j * Q$. As it's the convolutional result of the system impulse response H_{SIR} and channel impulse response H_{CIR} in time domain, the field measurement complex channel matrix of H_{CIR} can be calculated as:

$$\mathbf{H_{CIR}(t)} = \mathbf{IFFT\{H_{IR}(f)/H_{SIR}(f)\}} \quad (3)$$

2) Reconstructed CIR of 2D model: As the key parameter set $\{\tau_l, \upsilon_l, \mathbf{\Omega}_{Rx,l}, \mathbf{\Omega}_{Tx,l}, \mathbf{\Psi}_l^{2D}\}$, which denote the delay, doppler frequency shift, angle information at Rx, angle information at Tx and channel polarization component for the l^{th} path, respectively, can be extracted via SAGE from the field measurement CIR, a reconstructed CIR can be calculated based on the well known 2D fading channel model in ITU R M.2135 [12] and 3GPP SCM [5]

$$h_{us,l}^{2D}(t) = \sum_{m=1}^{M_l} \mathbf{\Gamma}_{Rx,u}^{2D}(\mathbf{\Omega}_{Rx,l,m}) \mathbf{\Psi}_{l,m}^{2D} \mathbf{\Gamma}_{Tx,s}^{2D}(\mathbf{\Omega}_{Tx,l,m}) e^{j2\pi\upsilon_{l,m}t}. \quad (4)$$

where the superscript $2D$ indicates that the electromagnetic wave propagates in the 2D space, and the subscripts l and m stand for the path and the subpath, respectively. M_l indicates the number of the subpaths for path l. Ignoring the impact of elevation domain, the polarization field component in vertical domain and horizontal domain for both Tx and Rx antenna pattern can be selected out from the antenna calibration file in accordance to the corresponding azimuth angle information ϕ_{Tx} and ϕ_{Tx} while the elevation angle information $\theta_{Tx,0}$ and $\theta_{Rx,0}$ are fixed values.

$$\begin{cases} \mathbf{\Gamma}_{Rx,u}^{2D}(\mathbf{\Omega_{Rx,l,m}}) = \begin{bmatrix} \Gamma_{Rx,u,V}(\phi_{Rx,l,m}, \theta_{Rx,0}) \\ \Gamma_{Rx,u,H}(\phi_{Rx,l,m}, \theta_{Rx,0}) \end{bmatrix}^{\mathbf{T}}, \\ \mathbf{\Gamma}_{Tx,s}^{2D}(\mathbf{\Omega_{Tx,l,m}}) = \begin{bmatrix} \Gamma_{Tx,s,V}(\phi_{Tx,l,m}, \theta_{Tx,0}) \\ \Gamma_{Tx,s,H}(\phi_{Tx,l,m}, \theta_{Tx,0}) \end{bmatrix}. \end{cases} \quad (5)$$

The channel polarization matrix $\mathbf{\Psi}_{l,m}^{2D}$ of the (l,m) subpath can be denoted as

$$\mathbf{\Psi}_{l,m}^{2D} = \begin{bmatrix} \psi_{l,m,V,V} & \psi_{l,m,V,H} \\ \psi_{l,m,H,V} & \psi_{l,m,H,H} \end{bmatrix}. \quad (6)$$

where the complex entry $\psi_{l,m,p_1,p_2}, p_i \in \{V,H\}$ represents the polarization gain between the p_1 polarization component to the p_2 polarization component of the (l,m) subpath.

3) Reconstructed CIR of 3D model: By utilizing the elevation domain in 3D MIMO, parameters θ_{Tx} and θ_{Rx} represent the elevation angle of departure (EAOD) and the elevation angle of arrival (EAOA), respectively. The angle information at Tx is defined as $\mathbf{\Omega}_{Tx} = \{\theta_{Tx}, \phi_{Tx}\}$, while the angle information at Rx is defined as $\mathbf{\Omega}_{Rx} = \{\theta_{Rx}, \phi_{Rx}\}$. The 3D polarization matrix $\mathbf{\Psi}_{l,m}^{3D}$ of the (l,m) subpath is denoted by

$$\mathbf{\Psi}_{l,m}^{3D} = \begin{bmatrix} \psi_{l,m,V,V} & \psi_{l,m,V,H} \\ \psi_{l,m,H,V} & \psi_{l,m,H,H} \end{bmatrix}. \quad (7)$$

Thus the 3D antenna pattern in vertical and horizontal domain for both Tx and Rx can be selected out from the antenna calibartion file in accordance to the angle information (ϕ_{Rx}, θ_{Rx}) and (ϕ_{Tx}, θ_{Tx})

$$\begin{cases} \mathbf{\Gamma}_{Rx,u}^{3D}(\Omega_{Rx,l,m}) = \begin{bmatrix} \Gamma_{Rx,u,V}(\phi_{Rx,l,m}, \theta_{Rx,l,m}) \\ \Gamma_{Rx,u,H}(\phi_{Rx,l,m}, \theta_{Rx,l,m}) \end{bmatrix}^T \\ \mathbf{\Gamma}_{Tx,s}^{3D}(\Omega_{Tx,l,m}) = \begin{bmatrix} \Gamma_{Tx,s,V}(\phi_{Tx,l,m}, \theta_{Tx,l,m}) \\ \Gamma_{Tx,s,H}(\phi_{Tx,l,m}, \theta_{Tx,l,m}) \end{bmatrix}. \end{cases} \quad (8)$$

Based on the channel parameters mentioned above, the CIR for the proposed 3D model from the transmitter antenna element s to the receiver antenna element u, for path l can be easily reconstructed as

$$h_{us,l}^{3D}(t) = \sum_{m=1}^{M_l} \mathbf{\Gamma}_{Rx,u}^{3D}(\mathbf{\Omega}_{Rx,l,m}) \mathbf{\Psi}_{l,m}^{3D} \mathbf{\Gamma}_{Tx,s}^{3D}(\mathbf{\Omega}_{Tx,l,m}) e^{j2\pi\upsilon_{l,m}t}. \quad (9)$$

IV. Capacity Calculation and Eigenvalue Distribution

A. Capacity calculation

To analyze the channel capacity of the wideband channel, the CIRs $\mathbf{H}(t,\tau)$ should be converted into the corresponding frequency transfer functions $\mathbf{H}(t,f)$ by applying the Fourier transform. Assuming that the $\mathbf{H}(j,k)$ is the sample of $\mathbf{H}(t,f)$, then

$$\mathbf{H}(j,k) = \mathbf{H}(t,f)\,|_{t=j\cdot\Delta t, f=k\cdot\Delta f} = \mathbf{H}(j\cdot\Delta t, k\cdot\Delta f) \quad (10)$$

where Δt and Δf are the sampling intervals in the time and frequency domains, respectively.

The channel capacity is one of the important metrics for the MIMO channel, it's calculated by [13]

$$C(t) = \frac{1}{B}\int_B \log_2 \det(I_U + \frac{\rho}{\beta^2 S}\mathbf{H}(t,f)\mathbf{H}^H(t,f))df \quad (11)$$

where ρ denotes the SNR and B is the bandwidth. For the discrete channel response $\mathbf{H}(j,k)$, an approximation can be given by

$$C(j) \approx \frac{1}{K}\sum_{k=1}^{K}\log_2 \det(I_U + \frac{\rho}{\beta^2 S}\mathbf{H}(j,k)\mathbf{H}^H(j,k)) \quad (12)$$

where K is the number of frequency bins of j^{th} time realization. β is a common normalization factor for all channel realizations in such that the average channel power gain is unitary as

$$\varepsilon\{\frac{1}{\beta}\|\mathbf{H}(j,k)\|_F^2\} = U \cdot S \quad (13)$$

where $\|\|_F^2$ denotes the Frobenius norm.

B. Eigenvalue distribution

As a direct embodiment of correlation, the distribution of eigenvalues for the channel correlation matrix R, as defined below, is worth studying.

---

1) Get the frequency response $\mathbf{H(f)}$ on the base of CIR: $\mathbf{H}$(f)=FFT$\{\mathbf{H}$(t)$\}$
2) Get the channel correlation matrix $\mathbf{R}$: $\mathbf{R}$=$\mathbf{H}$(f)$\cdot\mathbf{H(f)}^{\mathbf{H}}$
3) Get the eigenvalues of the channel correlation matrix: $\{\lambda_i$,i=1,2,...,Rank$\{\mathbf{R}\}\}$=Eigen$\{\mathbf{R}\}$
4) Sort the eigenvalues in a descending order and calculate as below : $r(j)$=$s(j)$/S, here $s(j)$=$\sum_{i=1}^{j}\lambda_i$, S=$\sum_{i=1}^{Rank\{\mathbf{R}\}}\lambda_i$

A larger cumulative ratio indicates the existence of main eigenvalues and a higher channel correlation.

V. Results and Analysis

A. Capacity results and analysis

The reconstructed CIR, including field measured, 2D channel and 3D channel, can be used to find the achievable capacity. These can then be used to compare 2D and 3D capacity cumulative distribution functions (cdf) (derived from CIR of equations (4) and (9), respectively) and the corresponding capacity derived from the measured CIR. This is illustrated in Fig. 3.

Observations show that the capacity of 3D channel fits the corresponding capacity of practical channel well both in China and NZ measurements. The 5% outage capacity results are listed in Table. II. As expected, obvious capacity gap exists between 2D and 3D channel capacity, the gain varies with measurement scenarios. In China measurement, the capacity gain is 5.12 bps/Hz with a 24.6% increase, highlighting the importance of the elevation domain. As the horizontal propagation distance in NZ measurement is much larger than that of China measurement, the elevation domain plays a less important role in channel propagation, thus the capacity gain in NZ measurement is smaller than that of China, harvesting 3.96 bps/Hz gain with only 16.7% increasement. Abundant scatters exist, a richer scattering in the long distance propagation channel will lead to a lower correlation, thus the absolute capacity in NZ measurement is almost 3.3 bps/HZ larger than that of China measurement. Therefore we conclude that the elevation domain impose great influence on channel capacity and it should be taken into consideration in channel modeling.

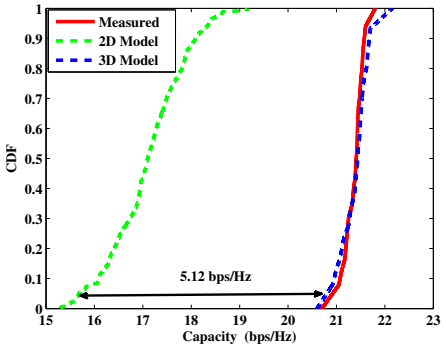

(a) Capacity in O2I scenario in China (SNR=5dB)

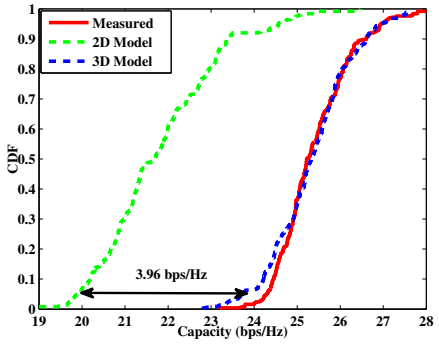

(b) Capacity in O2I scenario in NZ (SNR=5dB)

Fig. 3. Capacity in O2I scenario in China and NZ measurement

TABLE II
Capacity of 2D channel vs 3D channel vs field measurement

Case	2D channel (bps/Hz)	3D channel (bps/Hz)	Measured (bps/Hz)	Gain (bps/Hz)	Ratio (%)
China	15.68	20.80	20.94	5.12	24.6
NZ	19.87	23.83	24.21	3.96	16.7

B. Eigenvalue results and analysis

The cumulative ratio $r(j)$ (see Sec.II B) provides further insight for the distribution of eigenvalues. Here, we are interested at $r(4)$, $r(8)$, $r(16)$ and the CDF of them are illustrated in Fig. 4(a) and Fig. 4(b).

Looking at the first four eigenvalues, the summation of them with the 3D model better approximates the actual measurement. The cdf gap between the actual channel and the 2D channel is quite large. In 2D case the first four eigenvalues can be added to 70% of the total in China measurement and 60% in NZ measurement (50% cdf), thereby implying a dominant

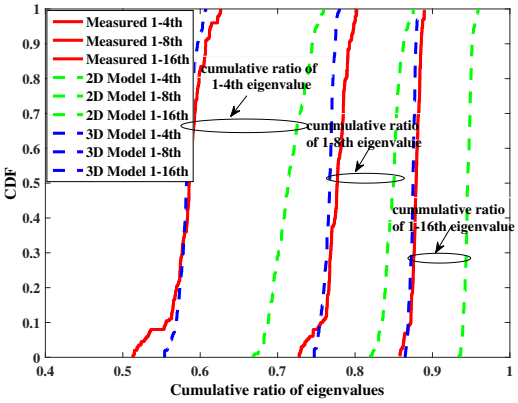

(a) CDF of cumulative ratio of eigenvalues in China.

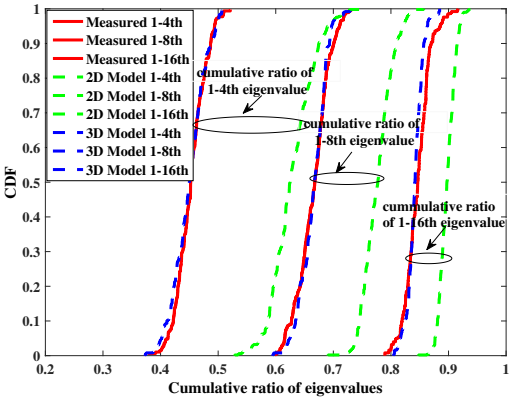

(b) CDF of cumulative ratio of eigenvalues in NZ.

Fig. 4. CDF of cumulative ratio of eigenvalues in China and NZ.

eigenvalue. Similar observations can be found when the first 8 and 16 eigenvalues are summed.

Further more, we plot the number of contributing eigenvalues, defined as those satisfying $E[\lambda_i] > 1$, under O2I scenario both in China and NZ in Fig. 5. Obviously, the number of contributing eigenvalues for 3D channel is larger than that of 2D channel, and close to that of field measurement, which is expected.

VI. Conclusion

In this paper, we constructed 2D and 3D CIRs from measurements, then presented comparative results of capacity and eigenvalues based on field measurements under O2I scenarios in China and NZ. We have validated the superiority of 3D MIMO over 2D on system capacity. Conclusions might be drawn that 3D channel approximates the practical channel well because their predicted capacity are stay closely, and 2D channel will heavily underestimate the capacity by neglecting the elevation domain. Eigenvalues are more evenly distributed for 3D channel, indicating a lower link correlation and a better channel scattering. All these results highlight the importance of elevation angle and contribute to a better understanding of 3D MIMO system design.

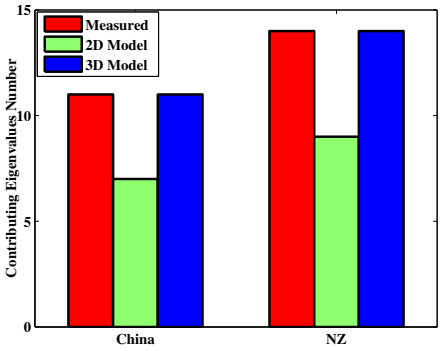

Fig. 5. Number of contributing eigenvalues in O2I scenario in China and NZ measurements

Acknowledgment

The research is supported by National Natural Science Foundation of China and project name is 'Theoretical Modeling and Experiment Research of Propagation Channel' with NO. 61322110. The author wish to thank Harsh Tataria for the helpful discussions.

References

[1] R.ITU, "Framework and overall objectives of the future development of IMT for 2020 and beyond," *San Diego,USA*, 10-18 June 2015.

[2] J. G. Andrews, S. Buzzi, W. Choi, S. V. Hanly, A. Lozano, A. C. Soong, and J. C. Zhang, "What will 5G be?" *Selected Areas in Communications, IEEE Journal on*, vol. 32, no. 6, pp. 1065–1082, 2014.

[3] J. Zhang, C. Pan, F. Pei, G. Liu, and X. Cheng, "Three-dimension fading channel models: A survey of elevation angle research," *IEEE Commun. Mag.*, vol. 52, no. 6, pp. 218 – 226, June 2014.

[4] T. Aulin, "A modified model for the fading signal at a mobile radio channel," *IEEE Trans. Veh. Tech.*, vol. 28, no. 3, pp. 182 – 203, 1979.

[5] H. Huang, "Spatial channel model for multiple input multiple output (MIMO) simulations," *3GPP TSG RAN, Edinburgh, UK, Tech. Rep. 3GPP TR*, vol. 25, no. 12.0, p. 0, 2004.

[6] M. Shafi, M. Zhang, P. J. Smith, A. L. Moustakas, and A. F. Molisch, "The impact of elevation angle on mimo capacity," in *Communications, 2006. ICC'06. IEEE International Conference on*, vol. 9. IEEE, 2006, pp. 4155–4160.

[7] Y.-H. Nam, B. L. Ng, K. Sayana, Y. Li, J. Zhang, Y. Kim, and J. Lee, "Full-dimension MIMO (FD-MIMO) for next generation cellular technology," *Communications Magazine, IEEE*, vol. 51, no. 6, pp. 172–179, 2013.

[8] J. Meinila, P. Kyosti, L. Hentila, T. Jamsa, E. Suikkanen, E. Kunnari, and M. Narandzic, "D5.3: WINNER+ Final Channel Models V.1," *Wireless World Initiative New Radio*, 2010.

[9] J. Koppenborg, H. Halbauer, S. Saur, and C. Hoek, "3D beamforming trials with an active antenna array," in *Smart Antennas (WSA), 2012 International ITG Workshop on*. IEEE, 2012, pp. 110–114.

[10] B. H. Fleury, M. Tschudin, R. Heddergott, D. Dahlhaus, and K. Ingeman Pedersen, "Channel parameter estimation in mobile radio environments using the SAGE algorithm," *IEEE J. Sel. Areas Commun.*, vol. 17, no. 3, pp. 434 – 450, 1999.

[11] J. Zhang, "Review of wideband mimo channel measurement and modeling for imt-advanced systems," *Chinese Science Bulletin*, vol. 57, no. 19, pp. 2387–2400, 2012.

[12] R. ITU, "M. 2135: Guidelines for evaluation of radio interface technologies for IMT-Advanced," 2008.

[13] D. P. Palomar, J. R. Fonollosa, and M. A. Lagunas, "Capacity results of spatially correlated frequency-selective mimo channels in umts," in *Vehicular Technology Conference, 2001. VTC 2001 Fall. IEEE VTS 54th*, vol. 2. IEEE, 2001, pp. 553–557.